



HAL
open science

Load transfer distribution in bolted-sealed joints

Minh-Nhat To, Eric Paroissien, Frédéric Lachaud, Valérie Nassiet, Bouchra Hassoune, Maëlen Aufray, Hélène Weleman

► **To cite this version:**

Minh-Nhat To, Eric Paroissien, Frédéric Lachaud, Valérie Nassiet, Bouchra Hassoune, et al.. Load transfer distribution in bolted-sealed joints. The Journal of Adhesion, 2024, 10.1080/00218464.2024.2303455 . hal-04402018

HAL Id: hal-04402018

<https://hal.science/hal-04402018v1>

Submitted on 18 Jan 2024

HAL is a multi-disciplinary open access archive for the deposit and dissemination of scientific research documents, whether they are published or not. The documents may come from teaching and research institutions in France or abroad, or from public or private research centers.

L'archive ouverte pluridisciplinaire **HAL**, est destinée au dépôt et à la diffusion de documents scientifiques de niveau recherche, publiés ou non, émanant des établissements d'enseignement et de recherche français ou étrangers, des laboratoires publics ou privés.



Distributed under a Creative Commons Attribution 4.0 International License

Load transfer distribution in bolted-sealed joints

Minh-Nhat To^{a,b,c}, Éric Paroissien^a, Frédéric Lachaud^a, Valérie Nassiet^b,
Bouchra Hassoune^b, Maëlénn Aufray^c, and Hélène Weleman^b

^aThe Clément Ader Institute, Université de Toulouse, ISAE-SUPAERO, INSA, IMT MINES ALBI, UTIII, CNRS, Toulouse, France; ^bLaboratoire Génie de Production (LGP), Université de Toulouse, INP-ENIT, Tarbes Cedex, France; ^cCIRIMAT, Université de Toulouse, CNRS, INPT, UPS, Toulouse, Cedex, France

ABSTRACT

Rubber-like materials such as sealant with recent developments in formulation are widely used in various structural components, especially in aerospace industry with many applications such as the sealing of bolted joints on aircraft. The objective of this paper is to assess the load transfer distribution in bolted-sealed joints through an approach coupling both experimental and numerical tests. Quasi-static and relaxation tests under uniaxial and pure shear loading were carried out to determine the parameters of phenomenological hyperelastic laws and of the generalized Maxwell model for the sealant PR 1782 C2. The fastener is an alloy steel bolt with a protruding head when the substrates are made from aluminum 2024-T3. Experimental and numerical quasi-static tests were then performed on double-lap bonded and bolted-sealed joints under in-plane loading. The numerical tests are done using 2D and 3D Finite Element (FE) models; they involve the visco-hyperelastic behavior previously assessed for the sealant. Accounting for visco-hyperelasticity makes it possible to better estimate the load transfer between bolt and sealant layer. Typically, the bolt load transfer rate is derived from numerical output for different sealant thicknesses. In the considered geometrical joint configuration, the sealant load contribution is between 7% and 13% according to the sealant thickness. Methodology and results provide a solid basis for the fatigue strength prediction of bolted-sealed joints.

KEYWORDS

Visco-hyperelastic constitutive law; experimental testing; uniaxial tensile test; pure shear test; double-lap bonded joint; finite element analysis; bolted-sealed joint; bolt load transfer rate

1. Introduction

Sealant finds widespread usage for multiple purposes, including sealing of bolted connections on airplanes. Bolted or riveted joints on aircraft structures may require a sealant layer in order to prevent corrosion induced by moisture absorption^[1] or to ensure the sealing of the cabin (such as the longitudinal joints of fuselage). Bolted-sealed joints can then be regarded as functionalized bolted joints, adding a sealing function to the mechanical function of load transfer, on which the fatigue strength is particularly dependent.^[2,3] Few studies are dedicated to the behavior of bolted-sealed assemblies in which

both bolt and sealant parts bring some mechanical contribution to the assembly mechanical resistance.

According to Atre's study,^[1] the joint's original design and fabrication process play a crucial role in determining the impact of the sealant on fatigue strength. Experimentally it was demonstrated that sealant had no effects on the fatigue resistance of thin sheet aluminum lap joints assembled by solid rivets since solid rivets perfectly fill the hole, the load is mainly transmitted by rivet shear. Static tests performed under low loading conditions for a comparison in terms of fatigue strength of double lap Hi-Lok riveted joints assembled with and without aeronautical sealant is presented by Boni and Lanciotti.^[4] Without preload, load transfer occurs through fastener shearing, and sealant does not significantly affect fatigue strength. However, when preload is applied, the load transfer is performed by friction, and adding sealant negatively impacts fatigue strength. In bolted joints, the presence of sealant layer helps to transmit part of the load but also affects the load transmitted by friction between the aluminum 7075-T73 substrates, leading to reduced fatigue strength.^[4] In some other researches, friction is not considered. Dechwayukul's^[5] and Kamnerdtong's works^[6] introduce the idea that the thin layer of polymeric sealant PR-1776-B2 inserted between contacting aluminum 7075-T6 surfaces, potentially supports a portion of the cyclic load and improves fatigue strength in riveted lap joints. It is discussed that if the stress concentration factor (dependent on load transfer) decreases, the fatigue life of the riveted-sealed joint would increase up to 2400%, indicating that the choice of sealant material and its properties significantly influence the joint's fatigue behavior. Bolted-sealed joints can then be regarded as special cases of hybrid (bolted/bonded) – termed HBB^[7] – joints involving very low-stiffness adhesives. A huge literature is dedicated to the mechanical behavior of HBB joints, where the considered adhesives exhibit significantly larger stiffness than a sealant. In that context, it was experimentally shown that a judicious choice for the adhesive can improve the quasi-static ultimate strength and the fatigue strength of HBB joints compared to the pure bonded or pure bolted corresponding joints.^[8-10] For instance, in the study of Kelly,^[11] an enhancement of more than 10 times in fatigue life at a load level equal to 50% of static failure load can be achieved when comparing HBB and pure bonded joints. Moreover, the one per one replacement of the sealant layer of a bolted-sealed joint by a stiffer adhesive layer can significantly improve the fatigue strength^[12] even enabling a reduction of 33% of the fastener rows.^[13,14] The fatigue strength improvement can be explained by the reduction of the stress concentration factor at fastener holes related to the reduction of both by-passed and transferred loads at fastener holes.^[5,13] The load distribution between the adhesive layer and fasteners is significantly dependent on the relative stiffness of the adhesive layer (joint design and/or adhesive material).^[10,15] Detailed and

simplified numerical models have been developed to assess the load distribution in HBB joints.^[15–18] Paroissien et al. developed an analytical model for the computation of bolt load transfer rate in HBB single-lap joints.^[13,19–21] According to this model (see Figure 18 in^[21]), the higher (respectively, lower) the adhesive shear stiffness, the lower (resp. higher) the bolt load transfer rate, so that HBB joint tends to behave, in terms of load transfer, more like as a pure bonded (resp. bolted) joint. Between these two extremal cases, the bolt load transfer rate is highly sensitive to the adhesive shear stiffness. It is important to note that this analytical model considers linear elasticity for the adhesive mechanical behavior, which does not correspond to the actual response of a sealant. Sealants are rubber-like materials and are then able to experience large deformation under small applied loads and to return to their initial shape without significant permanent deformation (below 0.2% offset of strain) after unloading.^[22] Because of their highly nonlinear stress-strain behavior, a classical modeling based on Lamé coefficient is not adequate. At the same time, rubber-like materials are known to exhibit time-dependent behavior, which means that their mechanical properties, such as stiffness and viscosity, can change over time. The behaviors of this kind of sealant must therefore be described by a visco-hyperelastic material model associating a hyperelastic model with viscoelastic response. The viscoelastic behavior of sealant can potentially affect the fatigue strength of the mechanical joint. As new sealant formulations may lead to transfer load in structural components, the study of these transfer load with the presence of visco-hyperelastic sealant is now necessary and was poorly reported. Regarding the simulation of bonded assemblies, hyperelasticity has already been taken into account within FE models, for instance on single-lap bonded or HBB joints.^[1,20,23,24] However, it is to note that the complex behavior of the sealant is not yet fully considered in studies while it would provide a better representation of the response of the sealant within the assembly and of related consequences on the macroscopic strength of the joint. The assessment of the mechanical behavior of highly deformable materials, such as flexible adhesives used within a joint under the shape of an adhesive layer, becomes complicated due to their inherent nonlinearities that can involve several dissipative phenomena and a width-to-thickness dependency.^[24–28]

The objective of this paper is then to present a methodology for the assessment of the load transfer in bolted-sealed joints through an approach coupling both experimental and numerical tests on bulk material specimens as well as on structural joints, while considering the sealant as a visco-hyperelastic material. The main focus of this paper is the assessment of load distribution in bolted-sealed joints as suitable parameters to better understand the joint potential fatigue strength improvement. Thus, any concern for fracture analysis is excluded. Moreover, a particular structural joint is considered in this paper: it consists in a double-lap joint with one slight-tightened

fastener. Despite the large use of the single-lap joint in the aerospace industry, this test suffers from several drawbacks: its mode mixity leads on uncertainty in numerical use of this test results. On the other hand, the peeling stress at overlap ends arising from the overlap bending induced by the neutral line lag is considerably reduced in double-lap configuration compared to single-lap configuration. In the case of the double-lap configuration, this reduction in peeling stress contributes to preventing the anticipated failure of the bonding agent.^[29,30] Besides, the slight level of preload applied prevents any load transfer by friction while the fastener preload, as well as interference fitting or cold working, is known as manufacturing technique to improve the fatigue strength of bolted joints.^[31] In this paper, the approach consists in (i) assessing the mechanical behavior of sealant on bulk specimens and then in (ii) validating on structural joints. The mechanical behavior of the sealant is modeled in the frame of the visco-hyperelasticity thanks to uniaxial tensile (UAT) and pure shear (PS) tests, under quasi-static and relaxation tests. The Mooney–Rivlin potential is used to model the hyperelasticity while the generalized Maxwell model is used for the viscoelasticity. The sealant is supposed as incompressible.^[22] Double-lap bonded and bolted-sealed joints with two different thicknesses (0.2 mm and 0.5 mm) of sealant are experimentally and numerically tested under quasi-static loading. The correlation between the experimental and numerical test results enables (i) the validation of the assessment of the sealant behavior and (ii) the determination of load distribution between the sealant and the fastener.

2. Experimental tests

2.1. Materials

The sealant material under study is the commercial reference PR 1782 C2³² supplied by PPG Aerospace, which is widely used in aeronautics. It is a two-part product based on cross-linking liquid polymer polysulfide with carbon dioxide manganese. The curing of such material lasts 12 hours in ambient condition.^[29] According to the dynamic mechanical thermal analysis (DMTA) on cured sealant ([Appendix 1](#)), the dependency of the shear modulus on the temperature range over which mechanical tests are performed ([18–24°C]) can be neglected. The substrates are made of aluminum alloys 2024-T3. In bolted-sealed joint, the steel alloys screw EN6115-3-5^[32] and nut ASNA2531-3 are used.

2.2. Specimen fabrication

The UAT test on PR 1782 C2 sealant is carried out with the dumbbell-shape specimen. The dumbbell specimens were manufactured using a specific

silicone mold. The specimens need de-bubbling as much as possible to avoid the inside defects. The bubbles inside the material caused by the mixing step were removed by placing it in a vacuum chamber. After that, the specimen is cured at laboratory temperature. The dimension of the specimen is designed according to ISO 37:2005(E) standard.^[33]

On the other hand, the PS test is designed with a rectangular specimen (section II.C.1). Samples were manufactured using two thin sheets with Teflon surface and a silicone frame as mold. After being de-gassed in the vacuum chamber, they were cured under high pressure for 12 hours at 30°C in a heating press again to minimize the porosity. The shearing behavior is observed in the edge (through-thickness plane) of the specimen. There are different dimensions of the rectangular specimen presented by researchers.^[34–36] The size of the testing area for pure shear specimen is chosen as $70 \times 10 \times 2 \text{ mm}^3$, same as the one used in the work of Meunier et al..^[34] For gripping in machine jaws, the global dimension of pure shear specimen is $70 \times 70 \times 2 \text{ mm}^3$.

The joint samples were manufactured using a steel mold that included specific spacers to control the dimension fitting and thickness of sealant layer. The sealant mixture is prepared beforehand using the supplier mixing procedure while the substrates are cleaned and degreased with acetone. A constant pressure was applied to the assembly during the curing of sealant. The actual thicknesses of sealant layer were measured as $0.15 \pm 0.02 \text{ mm}$ (for the 0.2 mm thick bonded configuration); $0.50 \pm 0.03 \text{ mm}$ (for the 0.5 mm thick bonded configuration); $0.20 \pm 0.01 \text{ mm}$ (for the 0.2 mm thick bolted-sealed configuration) and $0.55 \pm 0.02 \text{ mm}$ (for the 0.5 mm thick bolted-sealed configuration) using a digital caliper. These thicknesses were locally measured by subtracting the joint thickness at multiple locations from the theoretical adherend thicknesses, which have very small differences to the actual ones. The substrates of bolted-sealed joints were drilled with a hole diameter of 4.8 mm, leading to hole clearance of 0.04 mm. After trying different torque wrench values in the assembly process, the value of 1.7 N.m allows for a properly tightened bolted joint.

2.3. Experimental protocol and test results

2.3.1. Sealant PR 1782 C2 bulk tests

Quasi-static tensile tests on UAT and PS test specimens were performed using a tensile INSTRON machine with a load cell of 500 N. The specimen is clamped at both ends with a sandpaper to prevent sliding (Figure 1). Dedicated jaws were designed to grip the PS specimen (Figure 2).

The testing speed of the INSTRON machine is controlled by defining the displacement speed. Since the elastomeric behavior is very sensitive to the strain rate, a same strain rate for both tests has to be applied to

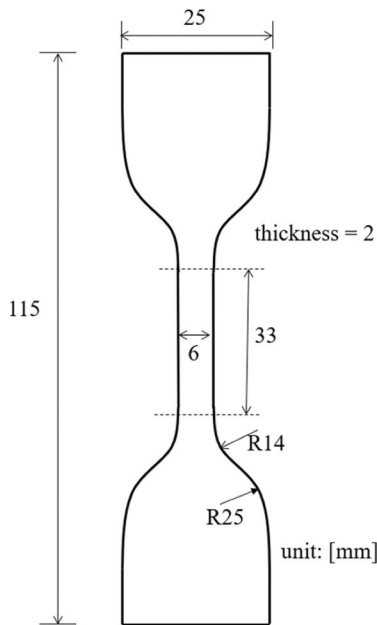


Figure 1. Uniaxial tensile test on a PR 1782 C2 dumbbell specimen.

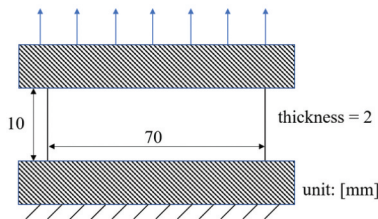


Figure 2. Pure shear specimen and test set-up.

ensure their results are connected. GOM Aramis 2 M digital image correlation system with an optical camera (1624×1236 pixels, 12 Hz maximum) is used to track the instantaneous local strain rate in each test region of interest. The specimen surface is marked with a silicone product to create the white and black points. The correlation camera makes it possible to track the relative displacement between points in the center of the specimen (highlighted by white squares with red border in [Figure 3](#)). The average true local strain rate is assumed to be the deformation speed of this square. Different values of machine test speed were considered for the UAT and PS tests. According to the correlation results, 0.065 s^{-1} for the local strain rate (or 0.07 s^{-1} of global strain rate) was selected,

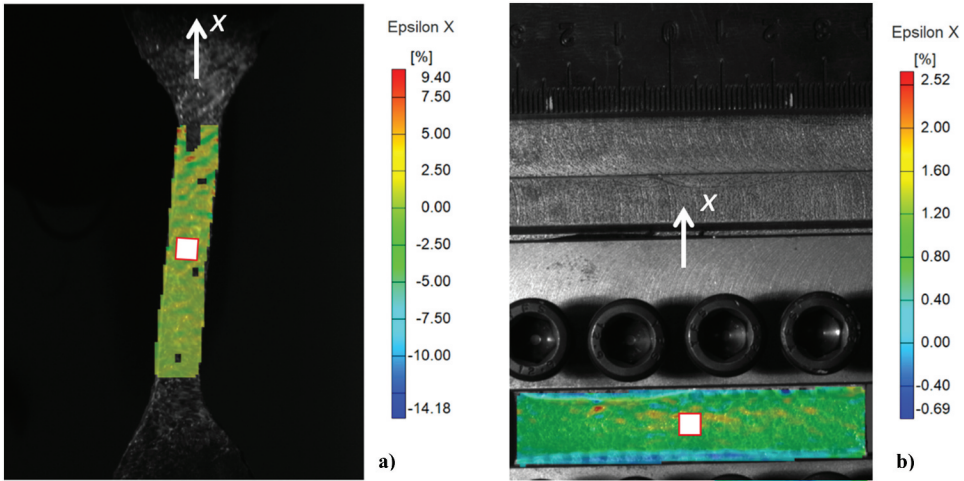


Figure 3. Longitudinal strain field on the PR 1782 C2 sealant obtained by digital images correlation: (a) UAT; (b) PS.

corresponding to 250 mm/min of machine speed for UAT test and 80 mm/min for PS test.

In both UAT and PS tests, the tensile Piola-Kirchhoff (PK1) stress σ is computed from the force as function of time recorded by the tensile machine divided by the area of the initial cross-section while the stretch λ is computed as the ratio of the actual length as function of time to the initial length of the specimen. In [Figures 4 and 5](#), the tensile PK1 stress σ as function of the stretch λ is provided for the UAT and PS test, respectively. Seven test cases were done for this quasi-static UAT test, and the repeatability of the results can be seen in [Figure 4](#). For quasi-static PS test, three test cases were conducted to observe the similarity of the test curves with maximum standard deviation on stress of around 15% ([Figure 5](#)). The experimental curves of UAT and PS tests are non-linear and the samples can experience large deformation.

In addition to quasi-static tests, the relaxation tests based on two previous configurations were also conducted to observe if the sealant material has any viscoelastic behavior. There are two stages for this kind of test: in the first stage, the displacement increases over time until the stretch ratio λ reaches 2 (strain $\varepsilon = 1$); after that, the strain is kept as constant and the machine continues to capture the reaction force of the test specimen. The test data of relaxation modulus as a function of time, computed as the ratio of tensile PK1 stress σ to the stretch ratio $\lambda = 2$, is shown in [Figure 6](#). As expected, the relaxation modulus decreases over time for both UAT and PS tests. While there is a difference between the two curves on the UAT samples, this difference remains consistent over time, and as a result, the values of the Prony series presented later (*see section III.C*) will not be affected.

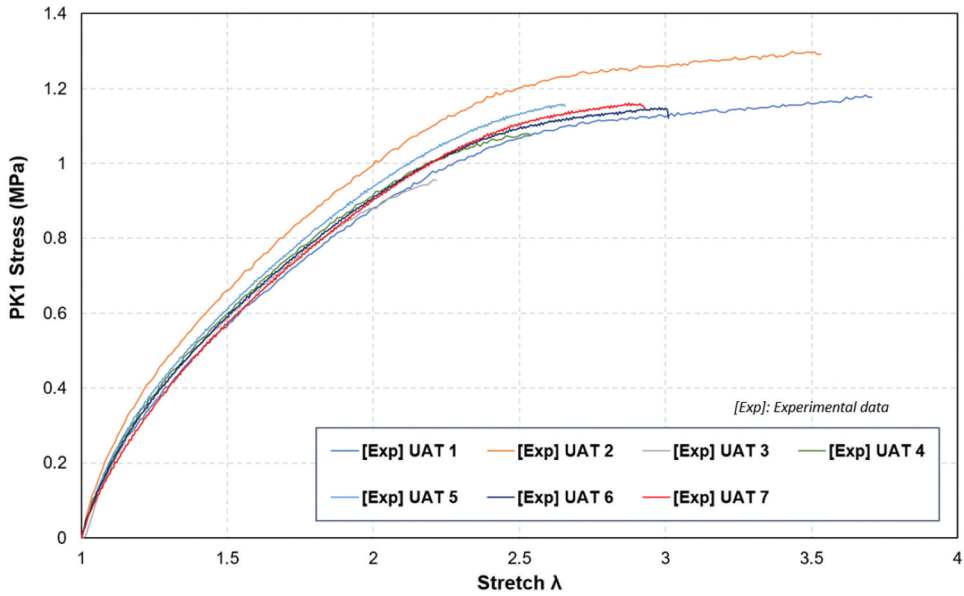


Figure 4. Experimental data for quasi-static UAT test on the PR 1782 C2 sealant (250 mm/min).

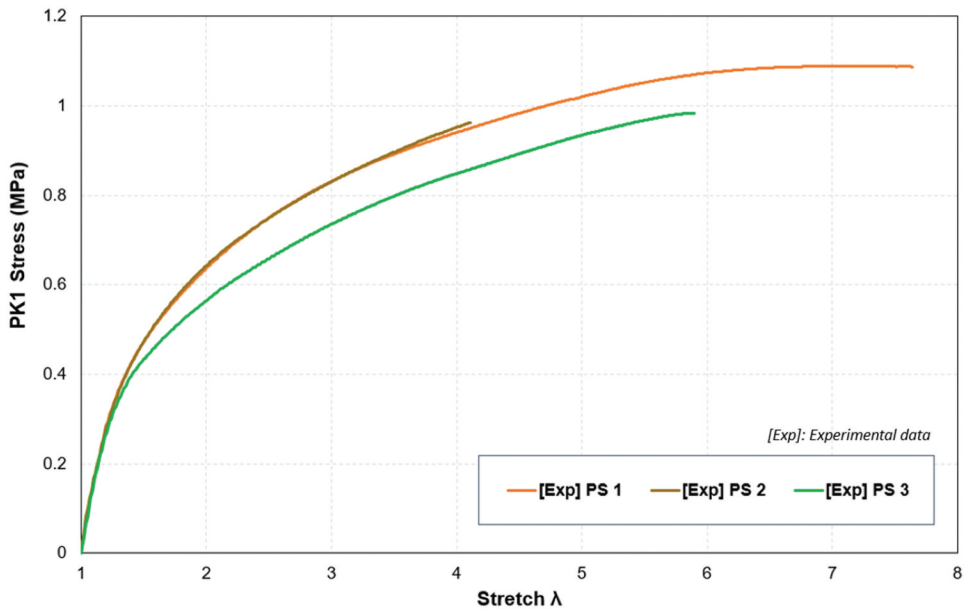


Figure 5. Experimental data for quasi-static PS test on the PR 1782 C2 sealant (80 mm/min).

2.3.2. Joint tensile tests

There are two configurations of joint that are involved: double-lap pure bonded and bolted-sealed joints with only one fastener. The geometry of the joints is described in [Figure 7](#) and [Table 1](#).

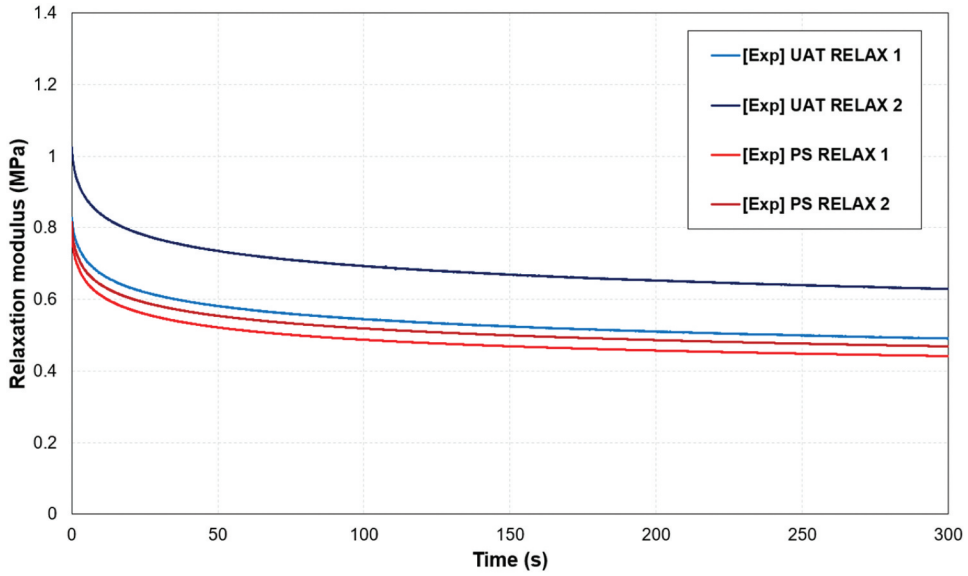


Figure 6. Experimental data for relaxation UAT and PS tests on the PR 1782 C2 sealant (stage at constant strain $\varepsilon = 1$).

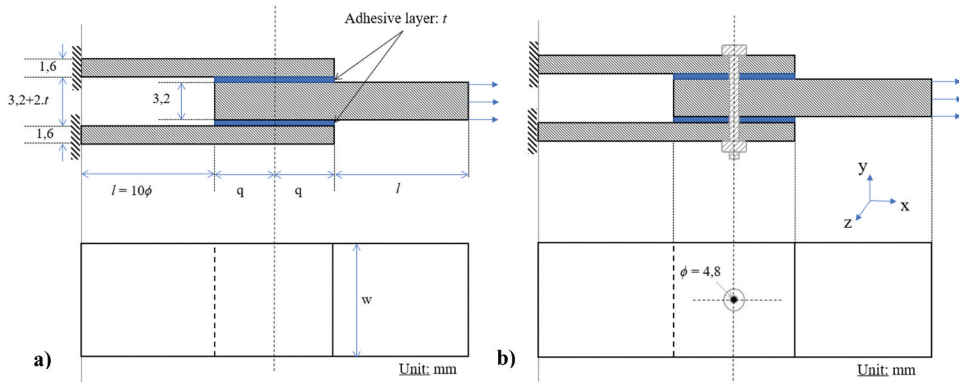


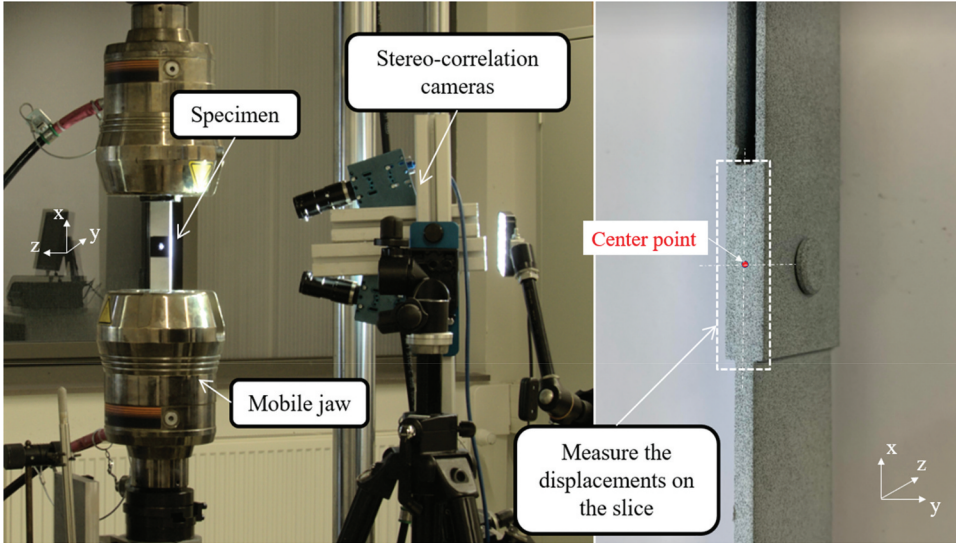
Figure 7. Geometry of pure bonded (a) and bolted-sealed (b) joints.

For these static tests, an increasing linear ramp load was applied until failure. The prescribed speed of the machine is set to 0,5 mm/min for both pure bonded and bolted-sealed tests.

The VIC3D/2D stereo-correlation system with two FLIR Grasshopper3 USB3 cameras at 43 FPS of frame rate with a 8.9 megapixel sensor (Figure 8) is used to determine the local displacement in the overlap of the joint which can be analyzed by tracking the movement of speckles surface. Two cameras were used to capture stereo-pair images of the joint from different angles that can be processed to compute 3D coordinates of

Table 1. Joint geometrical parameters.

l [mm]	q [mm]	w [mm]	t [mm]
48	14.4	28.8	0.2 or 0.5

**Figure 8.** Joint tensile test setup with stereo-correlation system.

the speckles points and calculate plane and out-of-plane displacements of the specimen during the test.

The force is measured by the tensile machine while the DIC allows for the measure of the axial displacement of a point located in the inner substrate at the middle of the overlap (see “center point” in Figure 8). This displacement is called local displacement. In Figures 9 and 10, the force as a function of the local displacement is given for the bonded joints and bolted-sealed joints, respectively, for both sealant thicknesses. The curve of the bonded joint can be divided into two parts: an increasing phase and a decreasing phase, the latter being attributed to the sealant failure. The lower the thickness, the greater the normal stresses imposed by the substrate on the sealant. Indeed, the sealant deforms less for the 0.2 mm configuration, which consequently results in greater stresses before the joint breaks. As the failure moment of sealant layer cannot be visibly detected from experimental test curves, the curve of the bolted-sealed joint looks like that of the pure bolted joint since the mechanical resistance of PR 1782 C2 sealant is low and the bolted behavior is dominant. For the bolted-sealed joint, four phases are observed on the force vs local displacement curves: (1) initial sliding, (2) almost linear force increase, (3) nonlinear force increase with a continuous stiffness decrease and (4) quasi constant force while the local

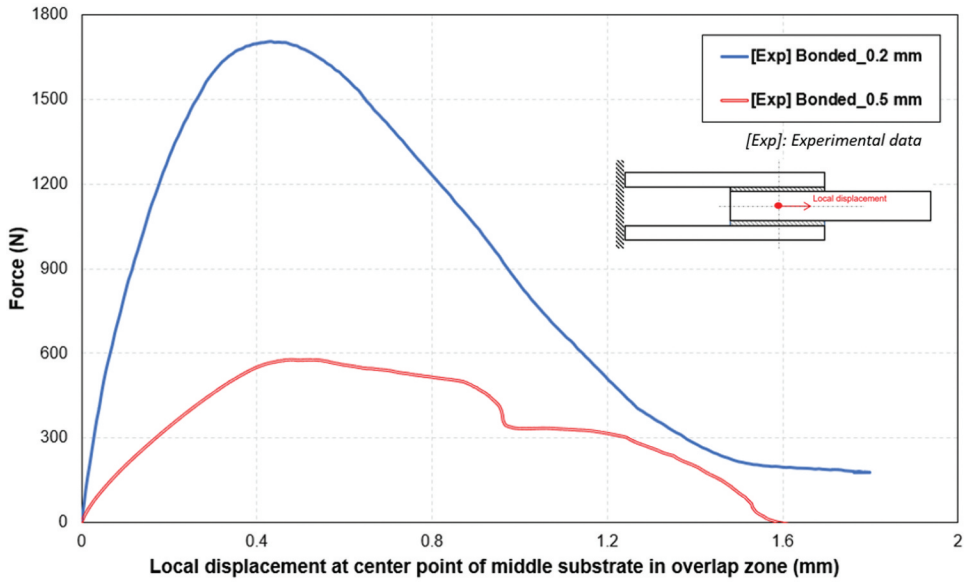


Figure 9. Experimental data of bonded joint: force versus local displacement for two different thicknesses of sealant layer.

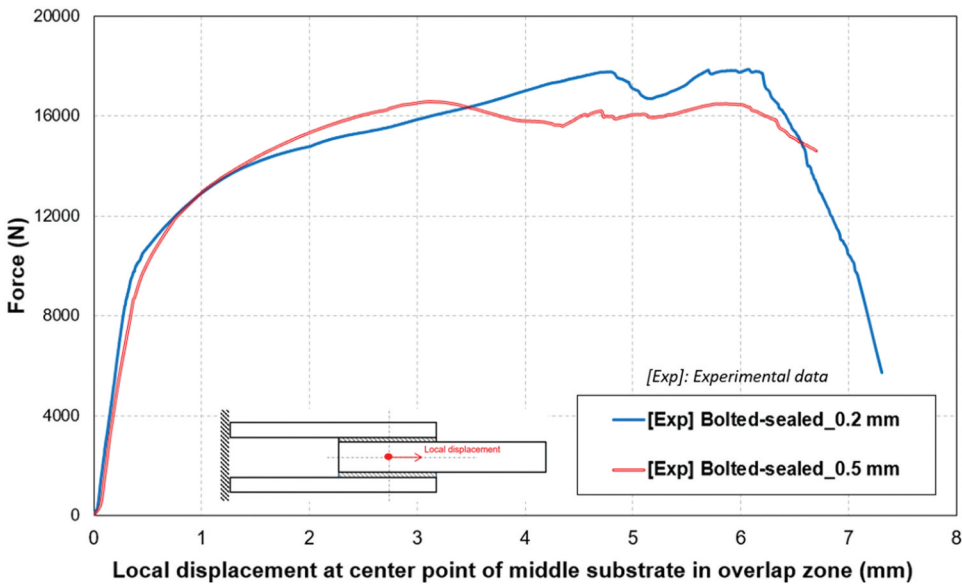


Figure 10. Experimental data of bolted-sealed joint: force versus local displacement for two different thicknesses of sealant layer.

displacement increases up to the final failure. This phase partition is typical of bolted joints^[37]: the first phase is associated to the clearance – not preceded by a friction transfer phase due to the slight pre-load applied – the second phase to the elastic transfer, the third phase to the plastic deformation due to bearing and

the fourth phase to the bearing degradation. Indeed, the relative low stiffness of the sealant leads to a mechanical behavior of the bolted-sealed joint dominated by the fastener.^[13,14]

3. Material parameters determination

3.1. Visco-hyperelastic constitutive laws

3.1.1. Mooney–Rivlin hyperelastic model

To account for the hyperelasticity of the sealant, the polynomial hyperelastic model can be used.^[28,38,39] The strain energy density function is a linear combination of two invariants of the left Cauchy – Green deformation tensor. Polynomial strain energy density function is given as:

$$W = \sum_{i,j=0}^n C_{ij}(\bar{I}_1 - 3)^i (\bar{I}_2 - 3)^j + \sum_{k=1}^m \frac{1}{D_k} (J - 1)^{2k} \quad (1)$$

where \bar{I}_1, \bar{I}_2 are reduced invariants of Green-LaGrange strain tensor, C_{ij} and D_k are material constants related to the deviatoric and volumetric response, respectively, $\kappa_k = \frac{2}{D_k}$ is the compressibility modulus in Pa while volumetric strain J is included in the model to account for the volume change of the material under deformation. In the present framework, the sealant is assumed incompressible, so that κ_k tends to infinity, D_k tends to 0 Pa⁻¹ and J tends to 1. When $n = 1$, the polynomial model is reduced to 2-parameter Mooney–Rivlin; when $n = 2$, the polynomial model is simplified to 5-parameter Mooney–Rivlin. The strain invariants $I_1 = \bar{I}_1/J^{-2/3}, I_2 = \bar{I}_2/J^{-4/3}$ can be expressed as functions of three principal stretches^[28,36]:

$$\begin{cases} I_1 = \lambda_1^2 + \lambda_2^2 + \lambda_3^2 \\ I_2 = (\lambda_1\lambda_2)^2 + (\lambda_2\lambda_3)^2 + (\lambda_1\lambda_3)^2 \\ I_3 = J = (\lambda_1\lambda_2\lambda_3)^2 \end{cases} \quad (2)$$

with λ_i is the principal stretch ratio in the direction i (with $i = 1, 2, 3$)

In uniaxial tensile test of incompressible material, it is assumed that $\lambda_2 = \lambda_3$, so:

$$\begin{cases} \lambda_1 = \lambda \\ \lambda_2 = \lambda_3 = \lambda^{-\frac{1}{2}} \end{cases} \quad (3)$$

Substituting (2) and (3) to the polynomial hyperelastic model (1), then taking its differential, the PK1 stress function for UAT, termed σ_{eng_UAT} , is obtained:

$$\begin{aligned} \sigma_{eng_UAT} &= \frac{\partial W}{\partial \lambda} \\ &= \sum_{i,j=0}^n 2C_{ij} \left(\lambda^2 + \frac{2}{\lambda} - 3 \right)^{i-1} \left(2\lambda + \frac{1}{\lambda^2} - 3 \right)^{j-1} \left[i \left(2\lambda^2 - 3\lambda - \frac{1}{\lambda} + \frac{3}{\lambda^2} - \frac{1}{\lambda^4} \right) + j \left(\lambda^2 - 3 + \frac{1}{\lambda} + \frac{3}{\lambda^3} - \frac{2}{\lambda^4} \right) \right] \end{aligned} \quad (4)$$

In PS test of incompressible material, it is assumed that $\lambda_2 = 1$.

$$\begin{cases} \lambda_2 = 1 \\ \lambda_1 = \frac{1}{\lambda_3} = \lambda \end{cases} \quad (5)$$

Similar to uniaxial approach, the PK1 stress equation for polynomial hyper-elastic model under planar loading, termed σ_{eng_PS} , is thus given by:

$$\sigma_{eng_PS} = \frac{\partial W}{\partial \lambda} = \sum_{i,j=0}^n 2C_{ij}(i+j) \frac{1}{\lambda} \left(\lambda^2 - \frac{1}{\lambda^2} \right) \left(\lambda^2 + \frac{1}{\lambda^2} - 2 \right)^{i+j-1} \quad (6)$$

The Mooney–Rivlin hyperelastic models with 2, 3, 4, and 5 coefficients are special cases of polynomial model.

3.1.2. Generalized Maxwell model for viscoelasticity

The generalized Maxwell model (or Zener model) is used for this sealant with one elastic arm and one or multiple Maxwell arm(s).^[40] The generalized Maxwell model is a mathematical representation of material that exhibits both viscous and elastic behaviors represented as a series of dashpots and springs, respectively, connected in parallel. The complexity of the material's behavior is determined by the quantity of dashpots (characterized by their relaxation time τ_i) and springs (defined by their modulus E_i) employed in the model, where an increase in the number of dashpots and springs results in a better representation of complex behavior. Such model is well suited to materials such as polymers as it accounts for different energy storage and dissipation phenomena occurring within the material over multiple timescales (motion of individual polymer chains or larger segments of the polymer).

In this research, the viscoelastic behavior is modeled by the generalized Maxwell model associated with Prony series.^[40] In this series, two parameters are mainly considered: g_i (shear relaxation modulus ratio) and τ_i (relaxation time). It is assumed that the time dependency of the spherical part can be neglected. For the generalized Maxwell model, the shear relaxation modulus ratio (g_i) equals to the ratio of elastic modulus in viscous arm i (E_i) to total elastic modulus ($E_\infty + E_1 + E_2 + \dots + E_n$).

$$g_i = \frac{E_i}{E(t=0)} = \frac{E_i}{E_\infty + \sum_{i=1}^n E_i} \quad (7)$$

As mentioned above, relaxation tests are performed to determine the viscoelastic parameters of Prony series. To model the viscoelastic material, the generalized model with n Maxwell arm(s) is used. The relaxation function of the viscoelastic model is given by^[40]:

$$E(t) = E_{\infty} + \sum_{i=1}^n E_i * e^{\frac{-t}{\tau_i}} \quad (8)$$

It should be noted that the Maxwell arms (in the cases with multiple viscoelastic arms) are named in the order of increasing relaxation time: $\tau_i < \tau_{i+1}$ ($1 < i < n-1$).

3.2. Assessment of hyperelastic parameters

3.2.1. Identification method

The identification process of hyperelastic parameters is performed with the least squares method from experimental test data. Due to the shape of Mooney–Rivlin equations, the optimization process is linear and the solution is unique. The results are optimized considering all the UAT and PS experimental test results. The Mooney–Rivlin hyperelastic models are identified with 2, 3, 4, and 5 coefficients. From PK1 stress equations under PS loading (equation (6)), it should be noticed that the Mooney–Rivlin constants cannot be separately determined from only PS data. Instead, only sum of $(C_{10}; C_{01})$ and sum of $(C_{20}; C_{11}; C_{02})$ can be predicted from PS experimental curves.

As mentioned in the objective of this research, the material parameters determined for UAT and PS intend to be used for joints under low loading to have a mechanical condition representative of the fatigue loading. In bonded and bolted-sealed joint tests, the sealant is subjected to shearing, emphasizing the need of taking into account the results of PS test. Then, the maximum tensile stretch that needs to be considered in optimization process of UAT and PS tests can be determined from the related ultimate simple shear stretch. At the ultimate applied force on the bonded joint with the thickness of 0.2 mm (see section II.C.2), the shear stretch applied to the sealant was measured to be equal to 1.7. On the bolted-sealed configuration, at an applied stress of 200 MPa which is considered to overpass the maximal stress for the limited endurance domain for the application, the shear strain was found approximately 1.8. Hence, the shear stretch range $[0; 1.8]$ in the simple shear transformation is considered. The first and second invariants for the simple shear ($I_{1,SS}$, $I_{2,SS}$), pure shear ($I_{1,PS}$, $I_{2,PS}$), and uniaxial tensile ($I_{1,UAT}$, $I_{2,UAT}$) transformations are expressed such as:

$$\begin{cases} I_{1,SS} = I_{2,SS} = 3 + \gamma^2 \\ I_{1,PS} = I_{2,PS} = 1 + \lambda^2 + \lambda^{-2} \\ I_{1,UAT} = \lambda^2 + 2\lambda^{-1}; I_{2,UAT} = \lambda^{-2} + 2\lambda \end{cases} \quad (9)$$

where γ and λ are the shear stretch in simple shear (SS) and tensile stretch in UAT/PS test, respectively. By imposing the equality of invariants between the SS transformation and the PS and UAT transformations, the tensile stretch range $[1; 2.25]$ is selected for the identification procedure on PS and UAT tests.

Table 2. Optimized Mooney–Rivlin parameters.

Number of coefficients of Mooney–Rivlin model	C_{10} [MPa]	C_{01} [MPa]	C_{20} [MPa]	C_{11} [MPa]	C_{02} [MPa]	Sum of squared differences [MPa ²]
2	0.3520	−0.1674				9.1949
3	0.4170	−0.1860	−0.0146			2.8986
4	0.4405	−0.2174	−0.0213	0.0087		2.8251
5	0.6373	−0.4259	0.2165	−0.7498	0.5231	2.0926

3.2.2. Results

The optimized parameters of Mooney–Rivlin hyperelastic models with 2, 3, 4, and 5 coefficients are shown in Table 2. Among these choices, 5-coefficient Mooney–Rivlin model which results in the smallest sum of squared differences is chosen for sealant material model. The comparison between these models and their agreement to the experimental test envelope are shown in Figure 11.

Model performance based on an identification only from PS has also been investigated. As anticipated, when the total values of $(C_{10}; C_{01})$ and $(C_{20}; C_{11}; C_{02})$ in equation (6) at $n = 2$ are kept constant, the difference between the PS curves that are optimized based on all UAT and PS data and the curves that are optimized only on the PS test data is zero. Indeed, PK1 stress functions for these two identification modes mathematically return the same. One of the coefficient solutions $(0.1013; 0.1013; -0.0027; -0.0027; -0.0027)$, which is optimized using only PS data, produces a PS numerical response very close to the response of the coefficients in the last row of Table 2, since the considering sums $(C_{10}; C_{01})$ and $(C_{20}; C_{11}; C_{02})$ are approximately equal (Figure 12). When simulating joint tests where the sealant is primarily deformed in shear mode, multiple sets of hyperelastic parameters of Mooney–Rivlin model with 5 coefficients are chosen randomly for sealant material modeling while ensuring that the sums $(C_{10}; C_{01})$ and $(C_{20}; C_{11}; C_{02})$ remain constant. As shown in Appendix A2, the FE results of double-lap bonded joint, which are force-displacement relation and peeling/shear stress distribution in sealant layer, remain the same for various sets of coefficients, provided that the sums are kept unchanged. This is an interesting result in terms of methodology for this research: only PS experimental data would be needed to predict the force transfer distributions. It is important to note that this conclusion applies exclusively to this PS phenomenological law.

3.3. Viscoelastic parameters

The optimization of couples $[E_i; \tau_i]$ in the equation (8) using the least squares method is non-linear. Following Williams,^[41] it is decided to choose the relaxation times: one relaxation time per time decade. The optimization is then performed at the same time on all the relaxation UAT and PS tests (*see*

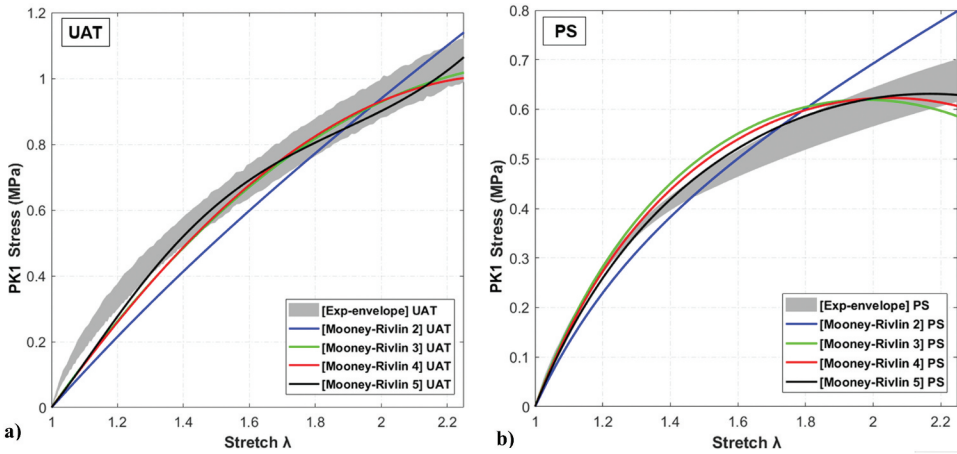


Figure 11. PK1 stress of 2, 3, 4, and 5-coefficient Mooney–Rivlin models for both UAT and PS tests.

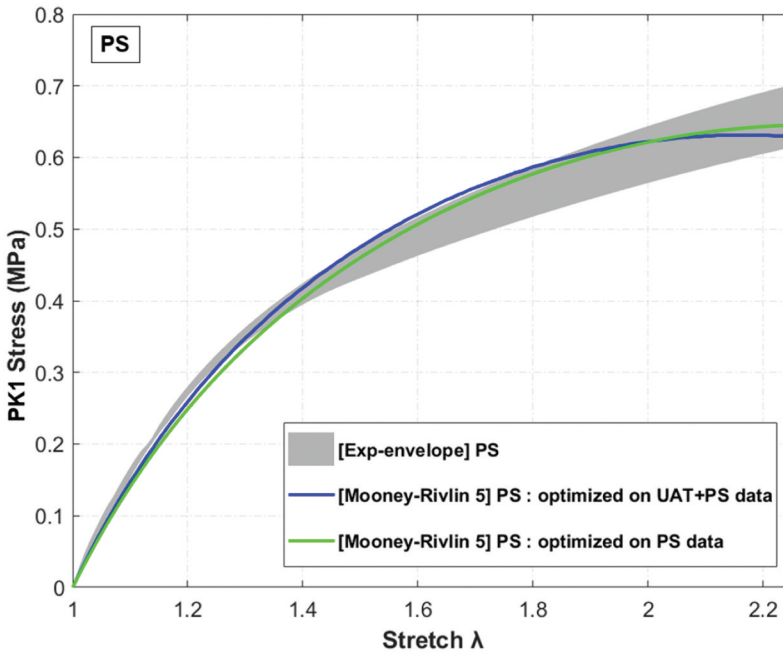


Figure 12. PK1 stress of PS test for 5-coefficient Mooney–Rivlin parameters optimized on both UAT and PS or only PS data.

section II.C.1). The values of infinite modulus E_∞ were determined as the values of the relaxation function at the end of each test, which gave an average modulus of 0.508 MPa for the model. Considering the period of time of relaxation tests, the three relaxation times are chosen $[\tau_1; \tau_2; \tau_3] = [1; 10; 100]$ second(s). Once the relaxation times are chosen, the optimization

Table 3. Calibrated prony parameters of 3-Maxwell-arm model.

Maxwell arm	E_i [MPa]	τ_i [s]	g_i
$i = 1$	0.0620	1	0.0725
$i = 2$	0.1382	10	0.1615
$i = 3$	0.1472	100	0.1722

becomes linear and the three corresponding moduli [E_1 ; E_2 ; E_3] are obtained (Table 3). The relaxation modulus responses of the generalized 3-arm Maxwell model for both UAT and PS tests are shown in Figure 13.

4. Finite element simulation

4.1. Numerical models

Now that the visco-hyperelastic parameters of the sealant have been determined, the objective is to integrate this modeling for the numerical study of purely bonded and bolted-sealed joints. FE simulations are performed using ABAQUS software. For the same bonded joint, 2D plane strain and 3D models are set for comparison purpose while 3D geometry is built for bolted-sealed joint. The geometries of bonded and bolted-sealed are given in Figure 7.

The adherends are made from aluminum alloys 2024-T3, while the bolt and nut are in steel alloys. The adhesive is the reference sealant PR 1782 C2. Linear elasticity is assumed for aluminum substrates and steel fastener. As for

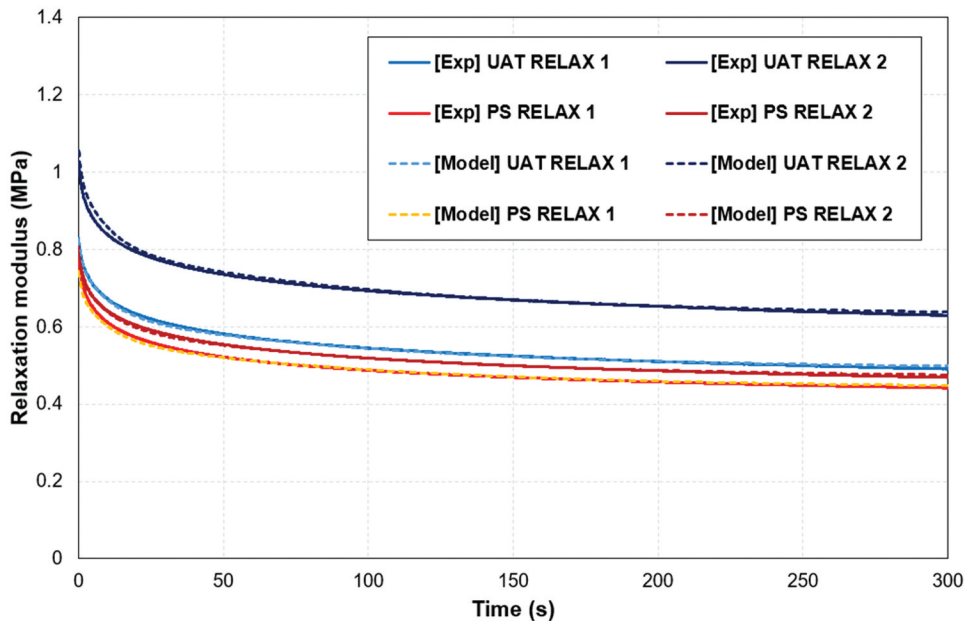


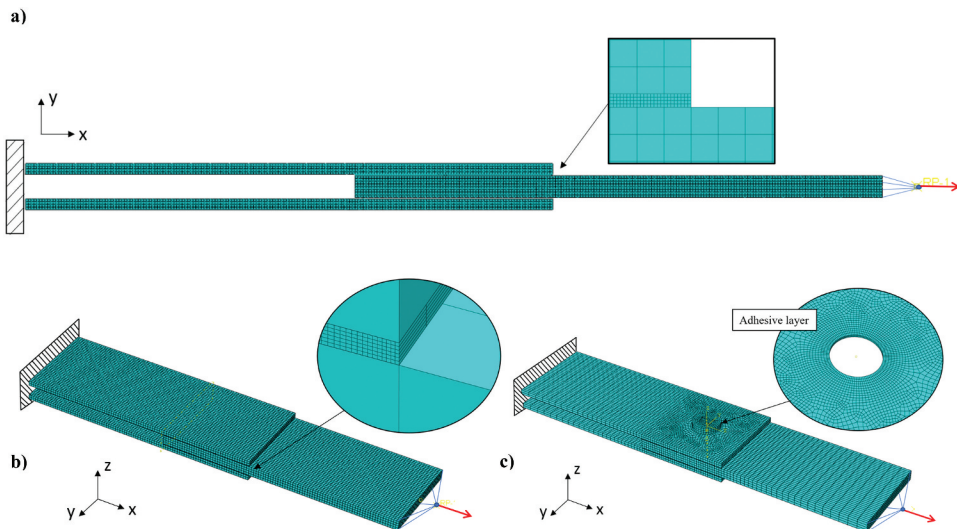
Figure 13. The modulus response of chosen generalized Maxwell model.

Table 4. Material properties of sealant for numerical simulation.

Visco-hyperelastic VHE	Parameters
Hyperelasticity: <i>5-coeff Mooney–Rivlin</i>	$(C_{10}; C_{01}; C_{20}; C_{11}; C_{02}) = (0.6373; -0.4259; 0.2165; -0.7498; 0.5231)$
Viscoelasticity: <i>Prony series</i>	$(E_i; \tau_i; E_2; \tau_2; E_3; \tau_3) = (0.0620; 1; 0.1382; 10; 0.1472; 100)$

experimental analysis, the attention will be given to numerical local displacement which makes it possible to neglect eventual metallic parts plastic behavior. Young's modulus of aluminum alloys and steel alloys are chosen as 72,000 and 210,000 MPa, respectively. Poisson's ratio for these metals is fixed at 0.33. In line with identification results of section III, the visco-hyperelastic model VHE for the sealant is considered in the simulation (Table 4).

The left side of the joint is clamped and the right side carries a surface displacement. In the numerical model, instead of applying the load directly to the surface, loading boundary condition is set on a spider node outside the joint which is kinematically coupled to target surface (Figure 14). This spider point is controlled at a displacement rate of 0.5 mm/min for both pure bonded and bolted-sealed configurations. The contact between the adherend and sealant is set as kinematics bonding contact (“tie contact” in ABAQUS). In bolted-sealed joint, the finite sliding surface-to-surface contacts with 0.3 of friction coefficient are used for bolt – hole contacts and no pre-load is applied for the bolt. It is indicated that only displacement rate is applied to the specimen. As the sealant layer behavior introduced in the FE model is visco-hyperelastic, the numerical test results are related to the displacement rate.

**Figure 14.** 2D & 3D joint meshes: bonded (a & b) and bolted-sealed (c) joints.

A further investigation could consist in varying the displacement rate applied for both numerical and experimental tests.

In this simulation, the Newton–Raphson method is used, which is a root-finding algorithm which produces successively better approximations to the roots of a real-valued function. In ABAQUS/Standard, the number of increments needed to find a converged solution for a load increment will vary depending on the degrees of nonlinearity in the system. Nonlinear geometric option is also enabled. For visco-hyperelastic material model, the Explicit/Implicit viscoelastic integration option is activated. The viscoelastic integration scheme determines how the time-dependent behavior of the material is provided into the simulation. The choice between explicit and implicit integration schemes will depend on the material behavior, the calculation duration, and the targeted level of computational efficiency and accuracy.

For the bonded joint, 2D elements are modeled under 2D plane strain assumption. Four-node bilinear element with two DOFs at node (element type CPE4 in ABAQUS) is used to mesh metallic components while the sealant element type is defined with enabled hybrid formulation (element type CPE4H in ABAQUS). For 3D models, the substrates and fastener are modeled with eight-node linear brick elements, with 3 degrees of freedom (DOF) at each node and fully integrated with $2 \times 2 \times 2$ integration points (element type C3D8 in ABAQUS). The element type of the sealant (element type C3D8H in ABAQUS) has similar definition to the previous one where enabled hybrid formulation option allows the element stiffness matrix to include both displacement and pressure variables. With different configurations of joint, the meshing strategies are different. For bonded models, the computation time is relatively short, which allows for a uniformly distributed mesh to be applied to all components. An even distribution of meshes in the sealant layer facilitates to establish a smooth stress distribution curve along the overlap. A mesh sensitivity study was done for 2D and 3D bonded configurations (see [Appendix A3](#)). The issue of convergence arises along with the increase of applied displacement and the convergence performance depends on the law identified. Without the presence of viscoelasticity, the calculation converges better. The chosen visco-hyperelastic material model with 5-coefficient Mooney–Rivlin parameters encounters convergence problem at specific displacement. Presented in,^[20] FE model with one element degree 2 in the sealant thickness was proposed to ensure the convergence of the simulation while giving good results in both local and global analysis. Using this method for 2D and 3D bonded configurations, the maximum applied displacement that leads to a converged calculation is around 0.7 mm for VHE. However, to extract the distribution of peeling/shear stresses in the middle of sealant layer, more than one element in the thickness is required. Therefore, the ultimate applied displacement at the right side of the joint is fixed at 0.15 mm (see [Appendix A3](#)). The global force-displacement relation is computed from reaction force and displacement of spider node that carries

load. For bonded joint, peeling and shear stresses in sealant layer are exported as average value of 2D/3D elements around each node in the neutral line of the sealant layer. Peeling and shear stress distributions are evaluated among various choices of mesh resolution. The chosen mesh not only has nearly asymptotic simulation results to the extremely fine meshed model, but also ensures that the calculation is converged. Additionally, finer mesh of sealant layer also provides more accurate stress distributions in the middle line. According to mesh study, the substrate mesh size for bonded model is chosen as 0.4 mm. For the sealant layer, the mesh size is 0.05 mm, corresponding to 4 elements in the thickness of 0.2 mm of sealant layer and 10 elements in the thickness of 0.5 mm.

In order to reduce the size of FE models of bolted-sealed joints, the mesh is oriented on purpose.^[20] The most important zone that needs to be observed is the overlap zone. In the same component, the mesh element size in this zone is considerably smaller than in others. With the presence of the hole, the pave meshing is applied to surrounding area [Figure 14\(c\)](#). The element size of sealant layer is adjusted to be as fine as possible but must still be respected in terms of calculation time (see [Appendix A3](#)). The bolted-sealed joint simulation experiences identical convergence issues as for the bonded case since the sealant layer has the same material model and dimensions, with or without a hole. For this reason, the limit of applied displacement leading to good convergence is fixed at 0.15 mm. In fact, when stress distributions are not of concern and only load transfer rate is important for fatigue applications, using a mesh with one element in the thickness can be a viable solution,^[20] especially when dealing with more complex sealant laws.

To compare accurately with the experimental test data, the sealant layers were modeled with their actual thickness. However, for more straightforward demonstration, the results and figures are indicated using the theoretical thicknesses: 0.2 mm and 0.5 mm.

4.2. Pure bonded joint

As shown in [Appendix A4](#), the 2D plane strain model is chosen since it is computationally faster while offering similar precision in global behavior to that of the 3D model.

For both thicknesses (0.2 mm and 0.5 mm) of bonded joint, experimental and numerical force – displacement results are provided in [Figure 15\(a\)](#). Specifically, the computational results involve local displacement at center point (see [Figure 8](#)) and visco-hyperelastic model (VHE) is compared to pure hyperelasticity with 5-coefficient Mooney–Rivlin model (HE). For the bonded configuration with 0.2 mm of sealant thickness, the difference between the numerical static stiffness and the experimental one is 14.33% with VHE and 39.12% with HE models. For the bonded configuration with 0.5 mm of sealant thickness, this difference comes, respectively, to 3.98% (VHE) and

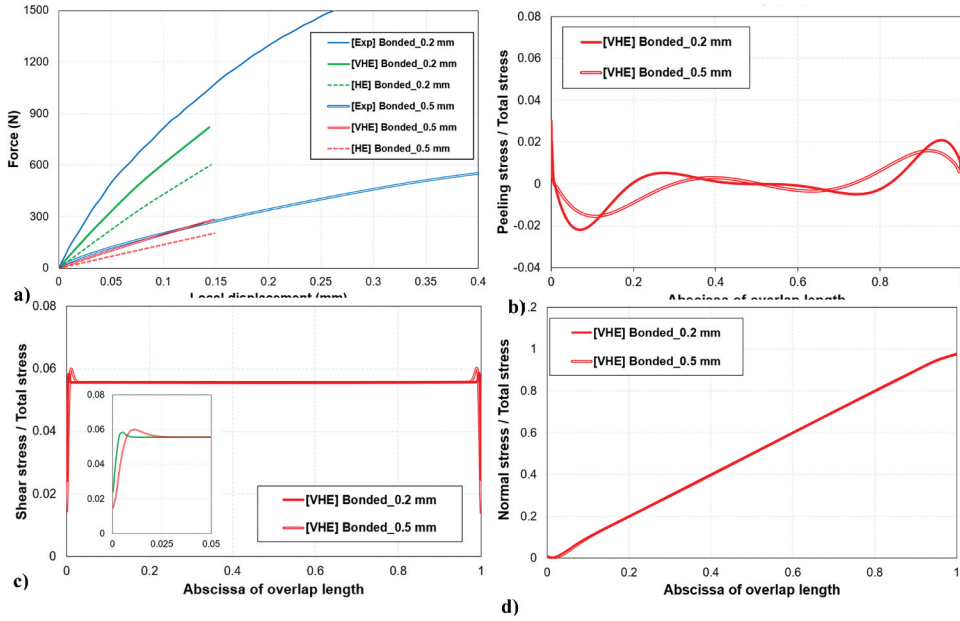


Figure 15. Configuration comparison 2D (VHE) – 0.2 vs. 0.5 mm of sealant thickness: (a) force vs. local displacement; (b) ratio of peeling stress to total stress in sealant layer; (c) ratio of shear stress to total stress in sealant layer; (d) ratio of normal stress in middle substrate to total stress.

20.27% (HE). The initial stiffness of the bonded joint thus clearly decreases if the viscoelasticity is not introduced in the sealant material, which shows the importance to account for the visco-hyperelasticity of the sealant to get a more realistic representation of the overall joint stiffness (see [Appendix A3](#)). Accordingly, further simulations provided in this work will consider the VHE model to represent the sealant mechanical behavior.

To go further in the understanding, the peeling and shear stresses are also exported in the midline of sealant layer (2D) or in the midline of symmetry plane (3D) to observe the distribution of stress.^[42] As shown in [Figure 15\(a\)](#), the maximum applied forces at 0.15 mm of global displacement are different for two cases with two values of sealant thickness, so the peeling/shear stresses are not directly comparable. The idea is to normalize these stresses by the applied stress, resulting in dimensionless quantities. Therefore, the comparison is conducted between the ratio of peeling/shear stress to the total applied stress at a given global displacement. The maximum applied stress is calculated by dividing maximum applied force by the loading surface area. Due to the flexibility of the sealant, the sealant shear stress is evenly distributed across the overlap, except at the end positions. Meanwhile, the peeling stress distribution is characterized by two distinct peaks located at some distance from the ends of the overlap. The peeling stress gradually decreases towards the central of the overlap ([Figure 15\(b, c\)](#)).

At last, it is interesting to investigate the influence of the sealant thickness on the stress distribution and global response of the joint. The same analysis approach is employed where the ratio of peeling/shear/normal stresses to the total applied stress is compared. According to Figure 15(b–d), the change of peeling stress distribution in sealant can be seen when the sealant thickness increases. Otherwise, shear stress and normal stress (in middle substrate) ratios are only slightly changed in the zone of overlap. It should be underlined that the numerical initial stiffness is well adapted to the experimental result for both configurations with 0.2 mm and 0.5 mm sealant thickness. Specially, the model with 0.5 mm of sealant thickness leads to lower initial stiffness than the 0.2 mm configuration. The lower the thickness, the greater the normal stresses imposed by the substrate on the sealant, and thus, the less deformation of the sealant layer.

4.3. Bolted-sealed joint

When the global displacement reaches 0.15 mm, the local displacement at center point (see Figure 8) is measured as around 0.12 mm. Figure 16(a) and Figure 17(a) show the local displacement – time relations at center point of middle substrate to observe the climbing slopes of experimental and numerical curves. As shown in Figure 16(b) and Figure 17(b), the initial stiffness of experimental and numerical curves are matching. The theoretical diameters of the bolt and the hole are, respectively, of 4.76 mm and 4.8 mm. The first slope thus corresponds to the joint movement for hole clearance. Regarding joint stiffness from second climbing slope, the bolted behavior is dominant. The difference between initial slopes of experimental and numerical curves is around 20%, which can be seen as acceptable.

The load carried by the bolt is provided as an output of the FE computation. For bolted-sealed joint with 0.2 mm of sealant thickness, 13% of applied load

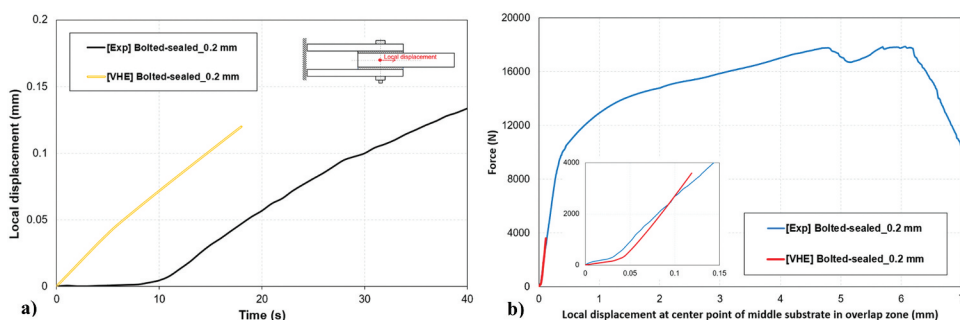


Figure 16. Bolted-sealed configuration 3D–0.2 mm of sealant thickness: (a) local displacement at central point as functions of time for an applied displacement of 0.15 mm; (b) force vs local displacement at central point.

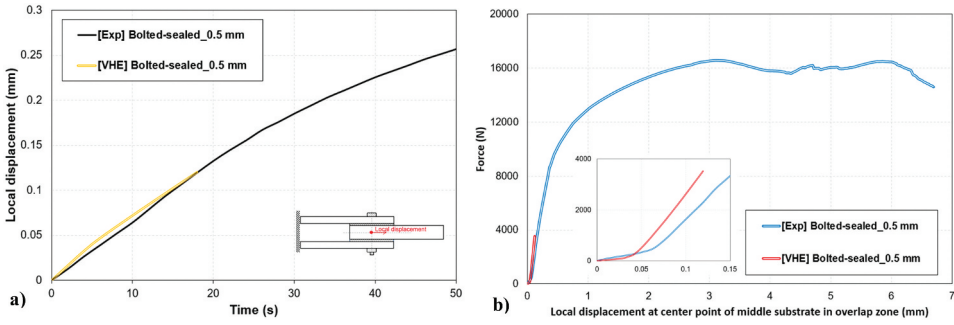


Figure 17. Bolted-sealed configuration 3D–0.5 mm of sealant thickness: (a) local displacement at central point as functions of time for an applied displacement of 0.15 mm; (b) force vs local displacement at central point.

goes in the sealant (Table 5). For bolted-sealed joints, the bolt and sealant layer both contribute on the load transfer. Accordingly, for a load of 4000 N applied to bolted-sealed joint (maximum value on Figure 16(b) for applied displacement of 0.15 mm), it means that 520 N is transferred by the sealant. When comparing this to the results of the bonded joint at 0.15 mm of applied displacement Figure 15(d), it is clear that the value of 520 N stands within the range of the joint applied force. With the same approach, for bolted-sealed joint with 0.5 mm of sealant thickness, 7% of applied load is transmitted through the sealant layer, that means at 3500 N of applied load, 245 N go in the sealant. The maximum level of applied force at 0.15 mm of displacement for the bonded joint with 0.5 mm of sealant thickness Figure 15(d) corresponds to 245 N. Referring to the experimental results of the joint with pure bonding (Figure 9), an applied load of 520 N (respectively, 245 N) is not far from the loading reached at 0.15 mm of displacement when the sealant thickness is 0.2 mm (respectively, 0.5 mm). As a result, the application of a maximal displacement of 0.15 mm to the bolted-sealed specimen in the FEM models appears as relevant to the identified material behavior for the sealant which does not take into account for degradation mechanism.

According to the load transfer rate of the bolt, it can be seen that the 0.2 mm-thick sealant layer in the bolted-sealed joint carries more load than the one in the configuration with 0.5 mm sealant thickness. The sealant can help to reduce the concentration of stresses at the joint interface and promote a more

Table 5. Bolted-sealed configuration –0.2 or 0.5 mm of sealant thickness (t): bolt load transfer rate for an applied displacement of 0.15 mm.

Sealant material model	Bolt load transfer rate τ (%)	
	$t = 0.2 \text{ mm}$	$t = 0.5 \text{ mm}$
VHE	87.00	93.44

even distribution of load and to contribute in improving the fatigue strength.^[5,20] The ability to assess the load transferred by the sealant, fatigue strength can be enhanced by modifying the joint design parameters to increase the load passing by the sealant layer: increase of the overlap area or reduction of plate thickness for example.^[13,15,18] Another possibility could be the strengthening of the sealant material by fillers addition.

5. Conclusion and perspectives

In this paper, a methodology for the assessment of the load transfer distribution in bolted-sealed double-lap joint is presented. The bolt load transfer rate is obtained from a numerical test on a refined non-linear 3D FE model of the bolted-sealed double-lap joint. The constitutive material behavior of the sealant introduced in the FE model is modeled in the frame of the visco-hyperelasticity. It is assessed thanks to relaxation and quasi-static elementary experimental tests on UAT and PS bulk specimens. Since the sealant layer is subjected to shearing in double-lap joint, the PS test results must be considered. The viscoelastic part is described thanks to Prony expansion series. The relaxed state is reached within the first 300 s and the relaxed modulus is 40% lower than the instantaneous modulus. A Mooney–Rivlin hyperelastic with five coefficients is identified through linear optimization, leading to a relaxed initial slope in shear of around 0.4 MPa. The reliability of the bolt load transfer rate determination is validated by correlating the force displacement curves at low loads, obtained experimentally and numerically (i) on both pure bonded and bolted-sealed double-lap joints and (ii) by considering two different sealant thicknesses. Indeed, as the stiffness of the sealant layer is very low, the global mechanical behavior of bolted-sealed joints is governed by the fastener. For the bolted-sealed double-lap joint considered, the bolt load transfer rate is around 13% (respectively, 7%) when the sealant layer thickness is 0.2 mm (resp. 0.5 mm), which is not negligible with regard to the very low sealant stiffness.

Besides, as this paper focuses on the influence of the sealant layer on the load transfer sharing within bolted-sealed joints under low loads, the use of common processes for fatigue strength enhancement such as preload, interference fitting, and cold expansions should be considered in conjunction with the sealant stiffening in next studies. Considering the case of aircraft bolted-sealed joints, the strengthening of the sealant material could be a way to improve their fatigue strength while keeping their initial functions. In the upcoming research, the presented methodology will be conducted for numerical assessment and comparison of fatigue improvement in both reference and reinforced sealants. Moreover, the present study focuses on double-lap configuration, preventing large peeling stress. The methodology presented in

this work could typically be expanded for the analysis of single-lap joint configuration often used in aircraft industry.

Nomenclature

C_{ij}	polynomial hyperelastic material coefficients (MPa)
D_k	compressibility coefficients (1/MPa)
E_i	elastic modulus (MPa) of Maxwell arm i
E_∞	elastic modulus (MPa) of elastic arm
g_i	shear relaxation modulus ratio of Maxwell arm i
I_i	invariants of Green-Lagrangian strain tensor
\bar{I}_i	reduced invariants of Green-Lagrangian strain tensor
I_i, SS	invariants of Green-Lagrangian strain tensor for simple shear transformation
I_i, PS	invariants of Green-Lagrangian strain tensor for pure shear transformation
I_i, UAT	invariants of Green-Lagrangian strain tensor for uniaxial tensile transformation $J =$ volumetric strain
l	substrate part outside the overlap (mm)
q	edge pitch of joint overlap (mm)
t	thickness of sealant layer (mm)
W	strain energy density (J/m ³ in SI)
w	joint width (mm)
κ_k	compressibility modulus (MPa)
λ_i	stretch in axis i
σ_i	stress in axis i (MPa)
τ_i	relaxation time (s) of Maxwell arm i
τ	bolt load transfer rate
ϕ	bolt diameter (mm)
Subscripts	
eng-PS	engineering stress under pure shear loading
eng-UAT	engineering stress under uniaxial loading
Abbreviations	
FE	Finite Element
HBB	Hybrid Bolted/Bonded
PS	Pure shear
UAT	Uniaxial tensile

Acknowledgments

The authors would like to acknowledge the sponsors of MIAM project, as well as the researchers and technicians at ISAE-SUPAERO Department of Mechanics, Structures and Materials (DMSM) and INP-ENIT Production engineering laboratory (LGP) for their supports and advices. The authors gratefully acknowledge Occitanie Region and Université Fédérale de Toulouse Midi-Pyrénées ISAE-SUPAERO.

Disclosure statement

No potential conflict of interest was reported by the author(s).

Funding

The work was supported by the Institut Supérieur de l'Aéronautique et de l'Espace Région Occitanie Pyrénées-Méditerranée.

References

- [1] Atre, A.; Johnson, W. S. Analysis of the Effects of Interference and Sealant on Riveted Lap Joints. *J. Aircr.* **2007**, *44*(2), 353–364. DOI: [10.2514/1.18320](https://doi.org/10.2514/1.18320).
- [2] Denkert, C.; Gerke, T.; Glienke, R.; Dörre, M.; Henkel, M. K.; Fricke, H.; Myslicki, S.; Kaufmann, M.; Voß, M.; Vallée, T. Experimental Investigations on Pre-Tensioned Hybrid Joints for Structural Steel Applications. *J. Adhes.* **2023**, *99*(2), 117–152. DOI: [10.1080/00218464.2021.2003786](https://doi.org/10.1080/00218464.2021.2003786).
- [3] Abeln, B.; Gessler, A.; Stammen, E.; Ilg, F.; Feldmann, M.; Dilger, K.; Schuler, C. Strengthening of Fatigue Cracks in Steel Bridges by Means of Adhesively Bonded Steel Patches. *J. Adhes.* **2022**, *98*(6), 6, 827–853. DOI: [10.1080/00218464.2021.2006059](https://doi.org/10.1080/00218464.2021.2006059).
- [4] Boni, L.; Lanciotti, A. Fatigue Behavior of Double Lap Riveted Joints Assembled with and without Interfay Sealant. *Fatigue Fract. Eng. Mater. Struct.* **2010**, *34*(1), 60–71. DOI: [10.1111/j.1460-2695.2010.01493.x](https://doi.org/10.1111/j.1460-2695.2010.01493.x).
- [5] Dechwayukul, C.; Rubin, C. A.; Hahn, G. T. Analysis of the Effects of Thin Sealant Layers in Aircraft Structural Joints. *Aiaa. J.* **2003**, *41*(11), 2216–2228. DOI: [10.2514/2.6814](https://doi.org/10.2514/2.6814).
- [6] Kamnerdtong, N., “The shear properties of a polymer sealant and analyses of the distortion and fatigue of sealed countersunk riveted lap joints”, PhD thesis, **2001**.
- [7] Hart-Smith, L. J. *Design Methodology for Bonded-Bolted Composite Joints*; Douglas Aircraft Company: Long Beach, California, **1982**; pp AFWAL-TR-81-3154.
- [8] Fu, M.; Mallick, P. K. Fatigue of Hybrid (Adhesive/Bolted) Joints in SRIM Composites. *Int. J. Adhes. Adhes.* **2001**, *21*(2), 145–159. DOI: [10.1016/S0143-7496\(00\)00047-6](https://doi.org/10.1016/S0143-7496(00)00047-6).
- [9] Sadowski, T.; Golewski, P.; Zarzeka-Raczkowska, E. Damage and Failure Processes of Hybrid Joints: Adhesive Bonded Aluminium Plates Reinforced by Rivets. *Comput. Mater. Sci.* **2011**, *50*(4), 1256–1262. DOI: [10.1016/j.commatsci.2010.06.022](https://doi.org/10.1016/j.commatsci.2010.06.022).
- [10] Bodjona, K.; Fielding, S.; Heidari-Rarani, M.; Lessard, L. Effect of Adhesive Layer Compliance on Strength of Single-Lap Hybrid Bonded-Bolted Joints. *Compos. Struct.* **Apr 2021**, *261*(1), 1–9. DOI: [10.1016/j.compstruct.2020.113324](https://doi.org/10.1016/j.compstruct.2020.113324).
- [11] Kelly, G. Quasi-Static Strength and Fatigue Life of Hybrid (Bonded/Bolted) Composite Single-Lap Joints. *Compos. Struct.* **2006**, *72*(1), 119–129. DOI: [10.1016/j.compstruct.2004.11.002](https://doi.org/10.1016/j.compstruct.2004.11.002).
- [12] Hartman, A. *Fatigue Tests on Single-Lap Joints in Clad 2024-T3 Aluminium Alloy Manufactured by a Combination of Riveting and Adhesive Bonding*. NLR-TN M2170 .1966, Amsterdam (NL): NTIS.
- [13] Paroissien, E., “Contribution aux Assemblages Hybrides (Boulonnés/Collés) – Application aux Jonctions Aéronautiques”. *PhD Thesis*, Université de Toulouse III Paul Sabatier (FR). **2006**. <http://thesesups.ups-tlse.fr/3/>.
- [14] Ramière, J. F.; Briançon, C.; Chéret, F.; Jeandrou, J. P.; Leroy, M.; Renard, J.; Thionnet, A. Jonctions hybrides boulonnées-collées. Application aux cas des structures d'avions. *Revue. des. composites. et. des. matériaux. avancés.* **2010**, *20*(2), 215–232. DOI: [10.3166/rcma.20.215-232](https://doi.org/10.3166/rcma.20.215-232).
- [15] Kelly, G. Load Transfer in Hybrid (Bonded/Bolted) Composite Single-Lap Joints. *Compos. Struct.* **2005**, *69*(1), 35–43. DOI: [10.1016/j.compstruct.2004.04.016](https://doi.org/10.1016/j.compstruct.2004.04.016).

- [16] Bois, C.; Wargnier, H.; Wahl, J.-C.; Le Goff, E. An Analytical Model for the Strength Prediction of Hybrid (Bolted/Bonded) Composite Joints. *Compos. Struct.* **2013**, *97*, 252–260. DOI: [10.1016/j.compstruct.2012.10.022](https://doi.org/10.1016/j.compstruct.2012.10.022).
- [17] Bodjona, K.; Raju, K.; Lim, G. H.; Lessard, L. Load Sharing in Single-Lap Bonded/Bolted Joints, Part I: Model Development and Validation. *Compos. Struct.* **2015**, *129*, 268–275. DOI: [10.1016/j.compstruct.2015.04.040](https://doi.org/10.1016/j.compstruct.2015.04.040).
- [18] Bodjona, K.; Lessard, L. Load Sharing in Single-Lap Bonded/Bolted Composite Joints. Part II: Global Sensitivity Analysis. *Compos. Struct.* **2015**, *129*, 276–283. DOI: [10.1016/j.compstruct.2015.03.069](https://doi.org/10.1016/j.compstruct.2015.03.069).
- [19] Paroissien, E.; Hoang-Ngoc, C. T.; Bhugaloo, H.; Ducher, D., Improving the Fatigue Life of Single-Lap Bolted Joints Thanks to the Hybrid (Bolted/Bonded) Joining Technology. 25th International Committee on Aeronautical Fatigue (ICAF 2009), Rotterdam, NL, Book of Proceedings, Springer Eds. ISBN 978-90-481-2745-0. pp. 475–492. May 27-29, 2009 doi: [10.1007/978-90-481-2746-7_27](https://doi.org/10.1007/978-90-481-2746-7_27)
- [20] Hoang-Ngoc, C. T.; Paroissien, E. Simulation of Single-Lap Bonded and Hybrid (Bolted/Bonded) Joints with Flexible Adhesive. *Int. J. Adhes. Adhes.* **2010**, *30*(3), 117–129. DOI: [10.1016/j.ijadhadh.2009.12.002](https://doi.org/10.1016/j.ijadhadh.2009.12.002).
- [21] Paroissien, E.; Lachaud, F.; Schwartz, S. Modelling load transfer in single-lap adhesively bonded and hybrid (bolted/bonded) joints. *Prog. Aerosp. Sci.* **2022**, *130*, 100811. DOI: [10.1016/j.paerosci.2022.100811](https://doi.org/10.1016/j.paerosci.2022.100811).
- [22] Brinson, H. F.; Brinson, L. C. *Polymer engineering science and viscoelasticity: an introduction*. Library of Congress ISBN. Springer. ISBN: 978-1-4899-7485-3. **2008**.
- [23] Crocker, L. E.; Duncan, B. C.; Hughes, R. G.; Urquhart, J. M., *Hyperelastic Modelling of Flexible Adhesives*; NPL Report CMMT(A)183. ISSN 1361-4061. May **1999**.
- [24] Lim, G. H.; Heidari-Rarani, M.; Bodjona, K.; Raju, K.; Romanov, V.; Lessard, L. Mechanical Characterization of EA9361 Flexible Epoxy Adhesive for the Design of Hybrid Bonded-Bolted Joints. *Polym. Test.* **2019**, *79*(106048), 1–9. DOI: [10.1016/j.polymertesting.2019.106048](https://doi.org/10.1016/j.polymertesting.2019.106048).
- [25] Lim, G. H.; Bodjona, K.; Raju, K.; Romanov, V.; Fielding, S.; Lessard, L. Evolution of Mechanical Properties of Flexible Epoxy Adhesives Under Cyclic Loading and Its Effects on Composite Hybrid Bolted/Bonded Joint Design. *Compos. Struct.* **2018**, *189*, 54–60. DOI: [10.1016/j.compstruct.2018.01.049](https://doi.org/10.1016/j.compstruct.2018.01.049).
- [26] Manterola, J.; Cabello, M.; Zurbitu, J.; Renart, J.; Turon, A.; Jumel, J.; Urresti, J. Effect of the Width-To-Thickness Ratio on the Mode I Fracture Toughness of Flexible Bonded Joints. *Eng. Fract. Mech.* **2019**, *218*, 106584. DOI: [10.1016/j.engfracmech.2019.106584](https://doi.org/10.1016/j.engfracmech.2019.106584).
- [27] Manterola, J. Development of Advanced Methods to Characterize the Fracture Behavior of Flexible Bonded Joints. *PhD. Thesis, Universitat de Girona (ES)*. **2020**. <http://hdl.handle.net/10803/672807>.
- [28] Cabello, M.; Zurbitu, J.; Renart, J.; Turon, A.; Martinez, F. A Non-Linear Hyperelastic Foundation Beam Theory Model for Double Cantilever Beam Tests with Thick Flexible Adhesive. *Int. J. Solids Struct.* **2015**, *80*, 19–27. DOI: [10.1016/j.ijsolstr.2015.10.017](https://doi.org/10.1016/j.ijsolstr.2015.10.017).
- [29] Hart-Smith, L. J. *Adhesive-bonded single-lap joints*; NASA Contractor Report, CR-112236, Douglas Aircraft Company: Long Beach (CA), **1973**.
- [30] Hart-Smith, L. J., *Adhesive-bonded double-lap joints*; NASA Contractor Report, CR-112235, Douglas Aircraft Company: Long Beach (CA), **1973**.
- [31] Benhaddou, T.; Stephan, P.; Daidie, A.; Alkatan, F.; Chirol, C.; Tuery, J. B. Effect of Axial Preload on Durability of Aerospace Fastened Joints. *Int. J. Mech. Sci.* **2018**, *137*, 214–223. DOI: [10.1016/j.ijmecsci.2018.01.023](https://doi.org/10.1016/j.ijmecsci.2018.01.023).
- [32] AECMA. *prEN6115-P5 (Aerospace Series, Bolts)*, European Association of Aerospace Industries; **2007**.

- [33] ISO 37:2005(E). *Rubber, Vulcanized or Thermoplastic: Determination of Tensile Stress-Strain Properties*
- [34] Meunier, L.; Chagnon, G.; Favier, D.; Orgeas, L.; Vacher, P. Mechanical experimental characterisation and numerical modelling of an unfilled silicone rubber. *Polym. Test.* **2008**, *27*(6), 765–777. DOI: [10.1016/j.polymertesting.2008.05.011](https://doi.org/10.1016/j.polymertesting.2008.05.011).
- [35] Moreira, D. C.; Nunes, L. C. S. Comparison of Simple and Pure Shear for an Incompressible Isotropic Hyperelastic Material Under Large Deformation. *Polym. Test.* **2013**, *32*(2), 240–248. DOI: [10.1016/j.polymertesting.2012.11.005](https://doi.org/10.1016/j.polymertesting.2012.11.005).
- [36] Sasso, M.; Palmieri, G.; Chiappini, G.; Amodio, D. Characterization of Hyperelastic Rubber-Like Materials by Biaxial and Uniaxial Stretching Tests Based on Optical Methods. *Polym. Test.* **2008**, *27*(8), 995–1004. DOI: [10.1016/j.polymertesting.2008.09.001](https://doi.org/10.1016/j.polymertesting.2008.09.001).
- [37] Guillot, J. Calcul des assemblages vissés. Assemblages de pièces planes de faibles épaisseurs. Partie 1. *Tech. de l'ingénieur. BM.* **2010**, *5564*, 1–20. DOI: [10.51257/a-v1-bm5564](https://doi.org/10.51257/a-v1-bm5564).
- [38] Mooney, M. A. A Theory of Large Elastic Deformation. *J. Appl. Phys.* **1940**, *11*(9), 582–592. DOI: [10.1063/1.1712836](https://doi.org/10.1063/1.1712836).
- [39] Rivlin, R. S.; Saunders, D. W. Large Elastic Deformations of Isotropic Materials VII. Experiments on the Deformation of Rubber. *Philos. Transactions. Royal Soc. London A.* **1951**, *243*(865), 251–288. DOI: [10.1098/rsta.1951.0004](https://doi.org/10.1098/rsta.1951.0004).
- [40] Brinson, L. C.; Gates, T. S. **2000**. *Comprehensive Composite Materials*. Elsevier Science
- [41] Williams, M. L. Structural Analysis of Viscoelastic Materials. *Aiaa. J.* **1964**, *2*(5), 785–808. DOI: [10.2514/3.2447](https://doi.org/10.2514/3.2447).
- [42] Paroissien, E.; Lachaud, F. On the Potential Static Strength of Hybrid (Bolted/Bonded) Lap Joints with Functionally Graded Adhesives. *Aiaa. J.* **2019**, *57*(2019), 4093–4103. DOI: [10.2514/1.J058372](https://doi.org/10.2514/1.J058372).

Appendix

A1. Dynamic mechanical thermal analysis of sealant

To monitor the mechanical behavior of the sealant under temperature, dynamic mechanical thermal analysis (DMTA) were registered on the 301 rheometer from Anton Paar, under air flow, using a rectangular configuration in shear dynamic mode. The testing specimen is made from sealant PR 1782 C2 under heating press to limit any possible inside defects and its dimension is $45 \times 10 \times 2$ mm³. The applied heating rate is 3°C/min from 15°C to 40°C. Therefore, the sealant which the glassy transition temperature is $-60^\circ\text{C} \pm 3^\circ\text{C}$ is tested in the rubbery state. The corresponding variation of storage G' and loss modulus G'' as a function of temperature is plotted in Figure 18.

Shear moduli of the sealant slightly change by varying testing temperature in the range of [15; 40] °C. Experimental quasi-static tests carried out on double-lap bonded and bolted-sealed and quasi-static and relaxation tests under UAT and PS loading on sealant samples were performed between 18°C and 24°C. Thus, the variation of the storage and loss moduli of the sealant are, respectively, less than 10% and 5% and are included in the experimental uncertainties. Consequently, the change in shear modulus in these cases can be neglected.

A2. Bonded numerical results for different 5-coefficient Mooney–Rivlin solutions

Three sets of hyperelastic parameters of Mooney–Rivlin model with five coefficients are proposed in Table 6 for the numerical verification in bonded joint simulations. These sets are chosen randomly while ensuring that the sums (C_{10} ; C_{01}) and (C_{20} ; C_{11} ; C_{02}) remain constant. The computational results of bonded joints are identical for these material models Figure 19.

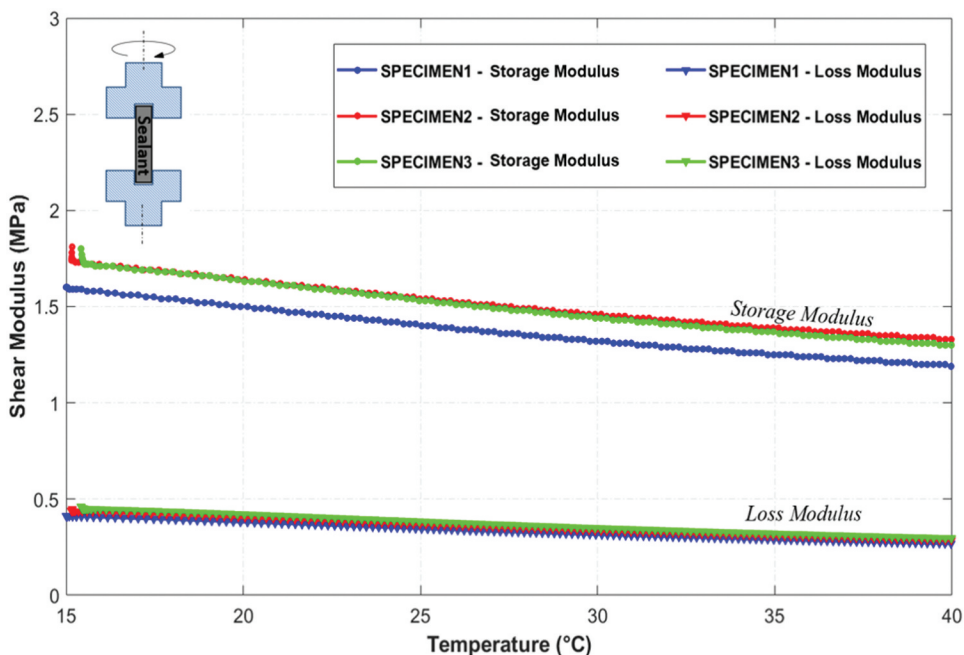


Figure A18. Dynamic mechanical thermal responses of the PR 1782 C2 sealant from 15 to 40°C.

Table A6. Different parameter sets for 5-coefficient Mooney–Rivlin hyper-elastic model.

Model	Mooney–Rivlin 5 coefficients
MR5_1	(0.6373; −0.4259; 0.2165; −0.7498; 0.5231)
MR5_2	(0.1000; 0.1114; 0.1000; 0.2000; −0.3102)
MR5_3	(−0.5000; 0.7114; −0.5000; 0.5000; −0.0102)

A3. Mesh sensitivity study for 2D bonded joints

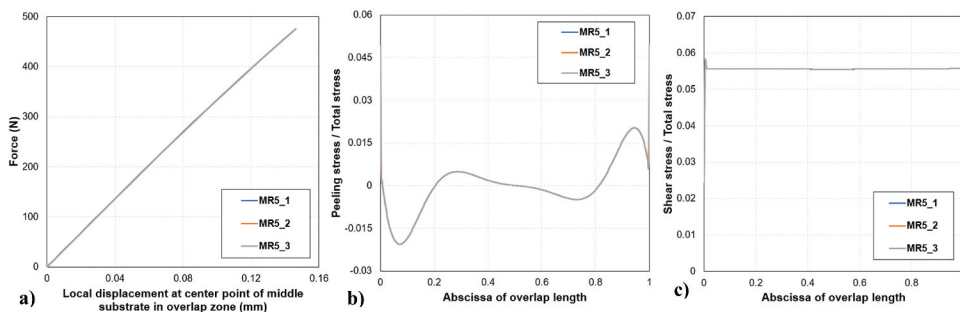
In this study, the mechanical behaviors in the sealant layer are highly concerned. The other parts, such as the substrates, do not require refined mesh. However, if the substrate mesh is too coarse, the result may be inaccurate. Therefore, with the same material model of sealant, 4 substrate mesh sizes are proposed to choose the appropriate mesh resolution for this case: 1.6, 0.8, 0.4 and 0.2 mm of substrate mesh size.

As shown in the [Figure 20](#), the mesh size does not have great impact on the peeling/shear stress distribution. The 0.4 mm of mesh size is nearly asymptotic to the most exact curve tested (0.2 mm) while requiring reasonable calculation time. Therefore, the 0.4 mm of mesh size is chosen for the substrate mesh size.

After choosing the appropriate mesh for the substrate, the mesh size of the sealant layer is then considered. For visco-hyperelastic VHE model, the calculation convergence depends on the number of elements in sealant thickness. With only one element in sealant thickness [20], the maximum applied displacement that leads to a converged calculation is around 0.7 mm for VHE. Without the presence of viscoelasticity, the calculation with pure hyperelastic sealant converges better ([Table 7](#)). The increase in the number of coefficients of Mooney–Rivlin model may provide unrealistic hyperelastic material behavior leading to instabilities at higher strains in the FE simulations. Although another material model may help improve convergence capability to go further in loading, from the point of view of the presented method, Mooney–Rivlin model with 5 coefficients would be relevant to assess the transfer at the level of loads applied. Moreover, the initial stiffness of the bonded joint decreases if the viscoelasticity is not introduced in the sealant material.

The influence of number of elements in sealant thickness on the local stiffness of the bonded joint is studied. When the number of elements in sealant thickness is varied, the initial stiffness undergoes only a minor change, which can be neglected ([Table 8](#)).

Four mesh resolutions, S2, S4, S6, and S8, are proposed with 2, 4, 6, 8 elements in the thickness of sealant layer of 0.2 mm, respectively. The peeling stress distributions in the sealant layer in 4 cases are shown in the [Figure 21](#). S4 and S6 are nearly asymptotic to the most exact curve (S8).

**Figure A19.** Bonded joint numerical results for different 5-coefficient Mooney–Rivlin solutions.

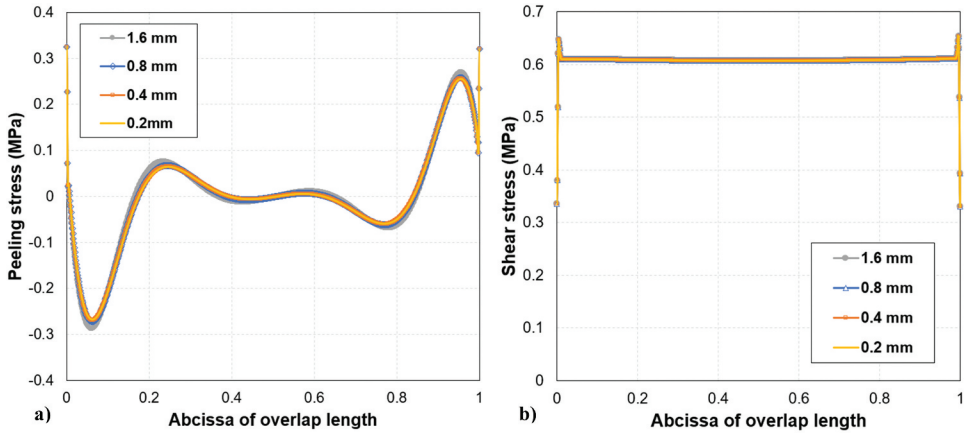


Figure A20. Peeling and shear stress distribution in sealant layer according to the substrate mesh size.

Table A7. Bonded configuration: maximum applied displacement for converged calculation for different number of elements in sealant thickness.

Number of elements in sealant thickness	1	2	3	4	5	6
Pure hyperelastic : HE (Mooney–Rivlin 5)	1.15	0.36	0.35	0.32	0.30	0.28
Visco-hyperelastic : VHE	0.7	0.15	0.15	0.15	0.15	0.15

Table A8. Bonded configuration (VHE): influence of number of elements in sealant layer to the joint initial stiffness.

Number of elements in sealant thickness	1	2	4	6	8
Initial stiffness (N/mm)	4405	4521	4546	4542	4557

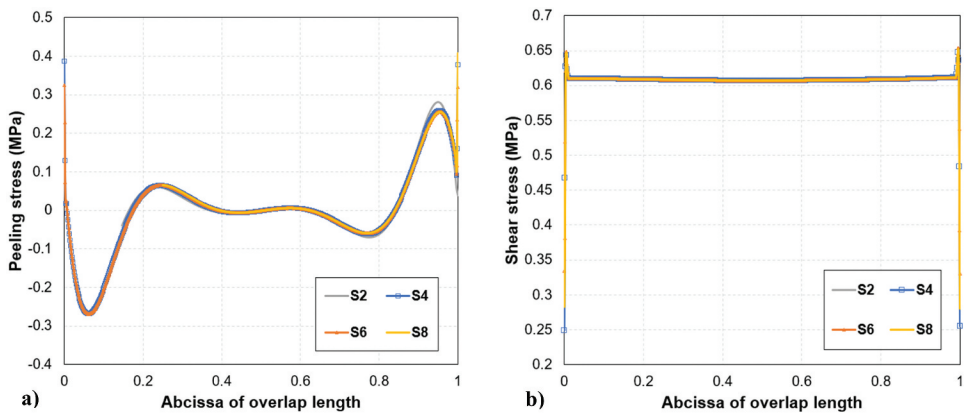


Figure A21. Peeling and shear stress distribution in sealant layer according to the substrate mesh size.

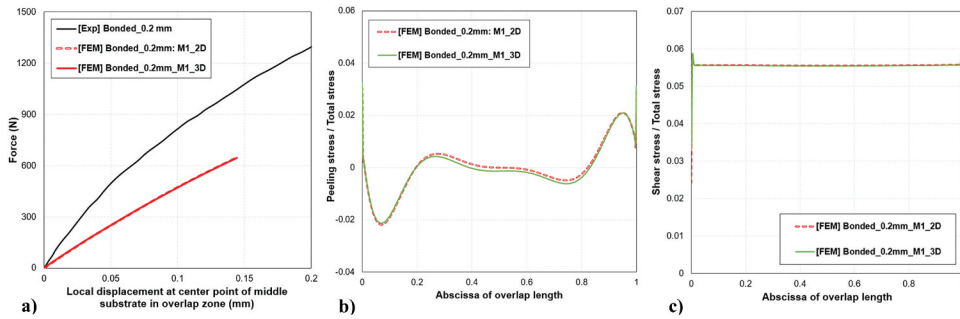


Figure A22. Comparison between 2D and 3D bonded models: (a) force – local displacement relation; (b) peeling stress distribution in sealant layer; (c) shear stress in sealant layer.

Therefore, the S4 with 4 elements in the sealant layer thickness of 0.2 mm is chosen because of the reasonable calculation time, simulation convergence and good distribution of stresses.

A4. Comparison between 2D and 3D bonded models

The 2D strain plane numerical model is calculated and its results are compared with the 3D results with a given set of sealant material parameters. In 3D simulation, the material is allowed to deform in all three dimensions, and this can lead to different stress and strain distributions compared to the 2D plane strain model, especially in the case with significant width. As shown in [Figure 22](#), the force – local displacement relation and peeling/shear stress distributions in middle line of sealant layer are almost the same. In conclusion, the 2D model is very useful in some cases because the calculation is faster and the results are acceptable with very small error compared to 3D refined FE models.